Magnetic domain-wall tilting due to domain-wall speed asymmetry

Dae-Yun Kim,[1] Min-Ho Park,[1] Yong-Keun Park,[1,2] Joo-Sung Kim,[1] Yoon-Seok Nam,[1] Hyun-Seok Hwang,[1]
Duck-Ho Kim,[1,*] Soong-Geun Je,[1,†] Byoung-Chul Min,[2] and Sug-Bong Choe[1,‡]
[1]*Department of Physics and Astronomy, Seoul National University, Seoul 08826, Republic of Korea*
[2]*Center for Spintronics, Korea Institute of Science and Technology, Seoul 02792, Republic of Korea*

(Received 16 November 2017; published 9 April 2018)

Broken symmetries in diverse systems generate a number of intriguing phenomena and the analysis on such broken symmetries often provides decisive clues for exploring underlying physics in the systems. Recently, in magnetic thin-film systems, the Dzyaloshinskii-Moriya interaction (DMI)—induced by the broken symmetry of structural inversion—accounts for various chiral phenomena, which are of timely issues in spintronics. Here, we report an experimental observation on unexpected tilting of magnetic domain walls (DWs) due to the broken symmetry under the application of the magnetic field transverse to the magnetic wire systems. It has been predicted that the DMI possibly causes such DW tilting in the direction of the energy minimization. However, very interestingly, experimental observation reveals that the DW tilting does not follow the prediction based on the energy minimization, even for the tilting direction. Instead, the DW tilting is governed by the DW speed asymmetry that is initiated by the DW pinning at wire edges. A simple analytic model is proposed in consideration of the DW speed asymmetry at wire edges, which successfully explains the experimental observation of the DW tilting directions and angles, as confirmed by numerical simulation. The present study manifests the decisive role of the DW pinning with the DW speed asymmetry, which determines the DW configuration and consequently, the dynamics.

DOI: 10.1103/PhysRevB.97.134407

I. INTRODUCTION

The Dzyaloshinskii-Moriya interaction (DMI)—antisymmetric exchange interaction [1,2]—has been actively studied nowadays due to its important role in spintronics by formation of the magnetic skyrmions [3–5] and stabilization of the chiral DWs [6,7]. Such DMI generates various phenomena of broken symmetries in magnetic systems, such as asymmetric domain expansion [8–10], asymmetric hysteresis loop [11], and asymmetric spin-wave propagation [12]. A recent theoretical study has predicted that the DMI also causes asymmetric DW tilting in the magnetic wire systems under application of in-plane magnetic field [13–15]. It is obvious that, due to the Zeeman interaction between the in-plane magnetic field and the magnetization inside the DW, the DW has to be tilted to an equilibrium angle of minimum-energy configuration. The equilibrium angle is thus determined by the counterbalance between the DMI and Zeeman energies. This prediction provides a DMI measurement scheme with a simple experimental setup. The present work is originally motivated to verify this prediction experimentally. For this study, the DW tilting is observed in various magnetic wire systems. However, surprisingly, the experimental observation exhibits completely different behavior apart from the prediction based on the energy minimization, even for the direction of the DW tilting. It is revealed that the DW tilting is governed by the symmetry [8] and/or additional asymmetry [16–22] of the chiral DW speed, which is initiated by the pinning process at the edges of wires. All the cases with/without the DMI and/or additional asymmetry are examined, which finally manifests unambiguously the decisive role of the DW speed asymmetry and the edge DW pinning [23,24] in the DW tilting phenomena.

II. SAMPLE FABRICATION AND EXPERIMENTAL SETUP

The sample structures are 2.5-nm Pt/0.9-nm Co/2.5-nm Cu/1.5-nm Pt (sample I), 4.0-nm Pt/0.3-nm Co/1.5-nm Pt (sample II), 2.5-nm Pt/0.5-nm Co/1.5-nm Pt (sample III), and 2.5-nm Pt/0.9-nm Co/2.5-nm Al/1.5-nm Pt (sample IV), respectively. These samples are chosen as the representatives of typical major properties: sample I (with DMI, but without chirality-induced asymmetry), sample II (without both DMI and chirality-induced asymmetry), sample III (without DMI, but with chirality-induced asymmetry), and sample IV (with both DMI and chirality-induced asymmetry). These samples were deposited by use of dc magnetron sputtering on Si substrates with 100-nm-thick SiO_2 and 5-nm-thick Ta buffer layers. After that, micromagnetic wire structures were manufactured by photolithography and ion-milling techniques. Magnetic domains were then observed by use of a magneto-optical Kerr effect microscope equipped with electromagnets, each of which can independently apply out-of- and in-plane magnetic field (H_z and H_x).

III. RESULTS

A. Observation of DW tilting induced by the DMI

To determine the DMI, the conventional technique proposed by Je *et al.* [8] is employed to measure the asymmetric DW

---

[*] Present address: Institute for Chemical Research, Kyoto University, Kyoto 611-0011, Japan.

[†] Present address: SPINTEC, Université Grenoble Alpes, CEA, CNRS, Grenoble INP, INAC-Spintec, Grenoble 38000, France.

[‡] Corresponding author: sugbong@snu.ac.kr

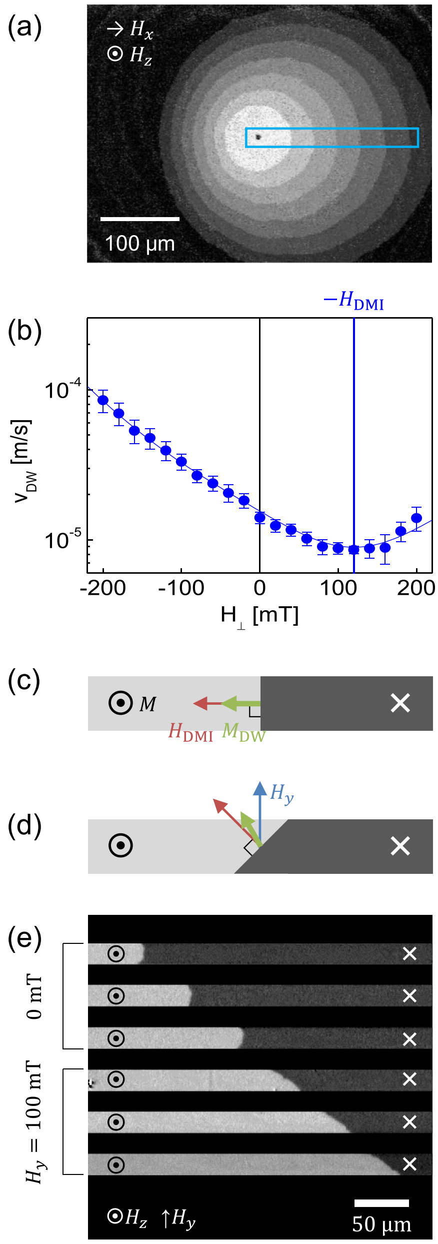

FIG. 1. (a) Successive image of asymmetrically propagating domain in continuous film under the application of H_z with H_x bias. Cyan box represents where the DW speed was measured. (b) Plot of v_{DW} as a function of $H_\perp$ under the application of constant $H_z = 10.3$ mT for sample I. It should be noted that the range of measured v_{DW} is of creep regime. The blue vertical line indicates $-H_{\mathrm{DMI}}$ (compensation field for the DMI-induced effective field). (b), (c) Schematic drawings of the DW configuration with a large negative H_{DMI} (c) without and (d) with application of H_y. The red, green, and blue arrows represent H_{DMI}, M (magnetization inside the DW), and H_y, respectively. (e) Image of the domains and DW for the microwire-patterned sample I. The first three and last three images show the propagating domain with and without application of H_y, respectively.

speed v_{DW}. As shown by Fig. 1(a), an asymmetric bubble domain expansion is observed under application of H_x and then v_{DW} is measured on the domain-wall (DW) segment (indicated by the cyan box) that is normal to H_x. Therefore, the present v_{DW} is purely governed by $H_\perp$, where $H_\perp$ is the applied in-plane field normal to the DW segment. Figure 1(b) plots v_{DW} with respect to $H_\perp$ for sample I. The plot clearly shows that v_{DW} has a minimum at $-H_{\mathrm{DMI}}$ (blue vertical line) and exhibits a symmetric variation with respect to this field, where H_{DMI} is the DMI-induced effective longitudinal magnetic field [6,8]. Therefore, H_{DMI} is quantified as -120 ± 5 mT for sample I.

Due to the large negative H_{DMI}, the magnetization M_{DW} inside the DW is aligned parallel to H_{DMI}, forming the left-handed Néel-type DW chirality as depicted in Fig. 1(c). If one applies an additional in-plane magnetic field H_y in the direction transverse to the wire, the Zeeman interaction will rotate M_{DW}, followed by tilting of the overall DW to keep the DW of left-handed Néel-type chirality [14]. For the present sample with a negative H_{DMI}, it is expected that the DW has to rotate clockwise under application of $H_y(>0)$ as shown by Fig. 1(d).

This prediction is, however, in contradiction to what is observed in the real experiment. Figure 1(e) shows the DW images after each successive application of out-of-plane magnetic field H_z pulses. The first three images were taken without application of H_y and the last three images were taken under application of H_y. The figure clearly shows the DW tilting between these two sorts of images, conforming that the tilting is truly caused by application of $H_y(>0)$. However, it is surprising to note that the direction of the DW tilting is counterclockwise, which is opposite to the prediction shown by Fig. 1(d). The present experimental observation, therefore, indicates that there should exist nother hidden governing factors in the DW tilting.

B. Mechanism of the DMI-induced DW tilting

It is interesting to note that the DWs with $H_y = 0$ show a shape of circular arcs, which indicate the existence of pinning at the edges of wire [23,24]. The subsequent effect from such arc formation can be explained as follows. Figure 2(a) depicts the typical DW shape of a circular arc. Due to the shape of arc, if one applies H_y (blue arrows), the component $H_\perp$ (black arrows) normal to the DW varies on position. Then, due to the v_{DW} dependence on $H_\perp$, v_{DW} also varies accordingly. For this sample, the upper and lower parts of the DW have positive and negative $H_\perp$, respectively, as shown by Fig. 2(a). Therefore, from the v_{DW} dependence on $H_\perp$ [Fig. 1(a)], the upper part moves slower than the lower part and consequently, the overall DW shape rotates counterclockwise. One can therefore conclude that the pinning effect can trigger the DW tilting, of which the direction accords to the experimental observation.

For better insight, we investigated the DW energy density σ_{DW} along the arc-shaped DW. According to Refs. [6,8], σ_{DW} is given as

$$\sigma_{\mathrm{DW}} = \sigma_0 + 2\lambda K_{\mathrm{D}}\cos^2\psi - \pi\lambda M_{\mathrm{S}} \times [(H_\perp + H_{\mathrm{DMI}})\cos\psi + H_\parallel \sin\psi], \qquad (1)$$

with the Bloch-type DW energy density σ_0, the DW width λ, the DW anisotropy energy density K_{D}, and the saturation magnetization M_{S}, where $H_\parallel$ is the component of H_y parallel to the DW and ψ is the angle of M_{DW} from the direction normal

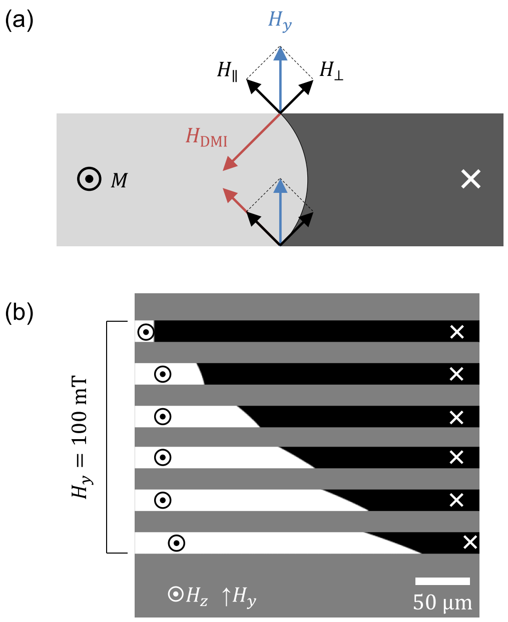

FIG. 2. (a) Schematic configuration of the arc-shaped DW due to the strong wire-edge pinning. The red and blue arrows represent $H_{\rm DMI}$ and H_y, respectively. The black arrows indicate the perpendicular and parallel components of H_y ($H_\perp$ and $H_\parallel$), respectively. (b) Numerical simulation results of the DW tilting.

to the DW. For general case, the equilibrium ψ is determined by the energy minimization condition for a given H_y.

Though there is no explicit analytic solution of Eq. (1) for the equilibrium ψ, one can roughly estimate $\sigma_{\rm DW}$ for the case of a large negative $H_{\rm DMI}$ as of sample I, since cos ψ is almost set to -1 and does not change much under the experimental range of H_y. For this case, one can readily obtain a simplified relation

$$\sigma_{\rm DW} \approx \sigma_0 + \pi\lambda M_{\rm S}(H_\perp + H_{\rm DMI}), \tag{2}$$

which manifests that $\sigma_{\rm DW}$ is mainly governed by total DW-normal magnetic field ($H_\perp + H_{\rm DMI}$). Since $v_{\rm DW}$ is faster for smaller $\sigma_{\rm DW}$ [8,25], one can therefore reach the same conclusion that the upper part of the DW with positive $H_\perp$ moves slower than the lower part with negative $H_\perp$ and consequently, the overall DW exhibit counterclockwise tilting.

C. Numerical simulation

To confirm the present prediction, we carried out a numerical simulation by including consideration of the local pinning force $f_{\rm pin}$. According to Refs. [25–27], the scaling constant α is proportional to $f_{\rm pin}$ in the creep criticality $v_{\rm DW} \propto \exp[-\alpha(\sigma_{\rm DW}/\sigma_0)^{1/4} H_z^{-1/4}]$ and thus one can replace α by $\alpha_0 f_{\rm pin}$, where α_0 is a constant irrespective of $f_{\rm pin}$. Then, $v_{\rm DW}$ depends now on $f_{\rm pin}$. In the simulation, $f_{\rm pin}$ is given by

$$f_{\rm pin} = \begin{cases} f_{\rm film} + \beta(y) f_{\rm edge} & \text{near edges} \\ f_{\rm film} & \text{otherwise} \end{cases}, \tag{3}$$

where $0 < \beta(y) < 1$, to mimic the edge pinning qualitatively, as shown by Fig. 3 (a). Meanwhile, the equilibrium value of $\sigma_{\rm DW}$ is obtained by applying minimization condition $\partial\sigma_{\rm DW}/\partial\psi|_{\psi=\psi_{\rm eq}} = 0$ to Eq. (1). In the calculation, all the typical material parameters were used as measured from sample I for the exchange stiffness $A(=22\ \mathrm{pJ/m})$, the effective uniaxial magnetic anisotropy $K_{\rm eff}(=5.7\ \times 10^5\ \mathrm{J/m^3})$, the saturation magnetization $M_{\rm s}(=1.4\ \times 10^6\ \mathrm{A/m})$, the DMI-induced effective field $H_{\rm DMI}(=-120\ \mathrm{mT})$, $v_0(=1.42\ \times 10^{14}\ \mathrm{m/s})$, and $\alpha_0(=13.28\ \mathrm{T}^{1/4})$.

In the simulation, the entire DW is divided into 200 segments along the wire width (20 μm) as shown in Fig. 3(b). The time interval for each iteration is set to keep the travel distance less than the length of the segments (0.1 μm). The ith lattice point at the nth iteration is denoted as (x_i^n, y_i^n) and then the next position is given by

$$\left(x_i^{n+1}, y_i^{n+1}\right) = \left(x_i^n + v_{\rm DW}\Delta t \cos\varphi_i^n,\ y_i^n + v_{\rm DW}\Delta t \sin\varphi_i^n\right), \tag{4}$$

where $\varphi_i^n = -\tan^{-1}\left(\frac{x_{i+1}^n - x_{i-1}^n}{y_{i+1}^n - y_{i-1}^n}\right)$. By repeating this procedure for every lattice point, one can obtain the contour of the DW at each iteration. Figure 2(b) shows the simulation results for the

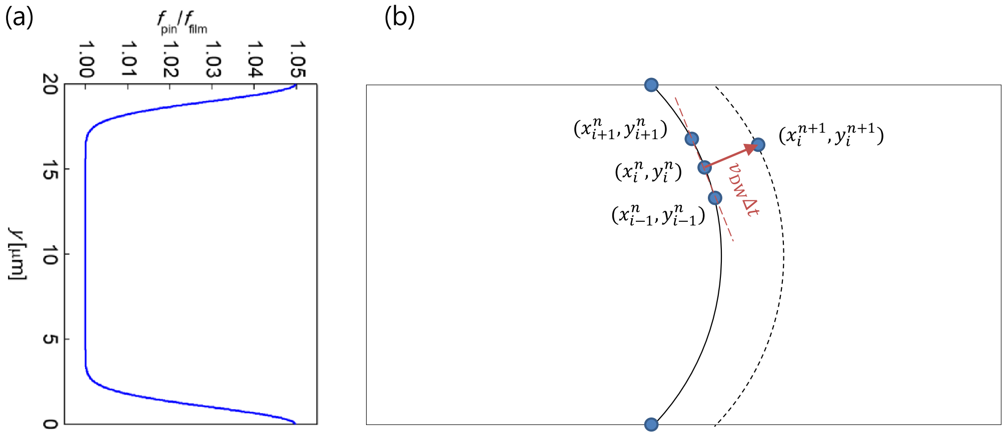

FIG. 3. (a) Plot of the ratio between $f_{\rm pin}$ and $f_{\rm film}$ as a function of position y, where $f_{\rm film}$ represents the value of $f_{\rm pin}$ at the center of the magnetic wire. (b) Schematic diagram of the numerical simulation. The blue dots represent the lattice points, and black solid and dashed lines indicate the DW at nth and $(n+1)$th iteration, respectively.

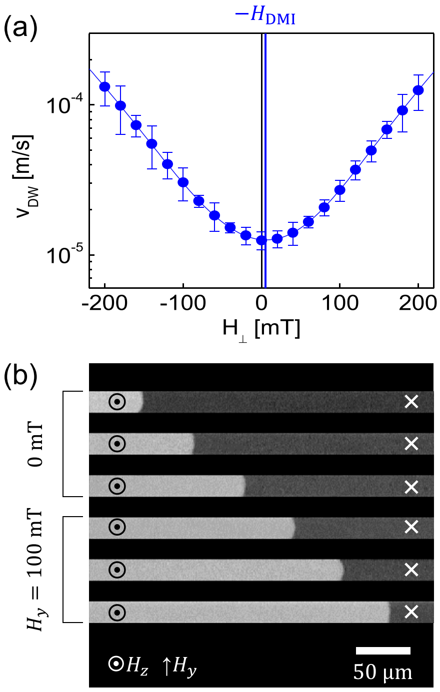

FIG. 4. (a) Plot of v_{DW} as a function of $H_{\perp}$ for sample II. The blue vertical line indicates $-H_{\mathrm{DMI}}$. (b) Image of the domains and DW for the microwire-patterned sample II. The first three and last three images show the propagating domain without and with application of H_y, respectively.

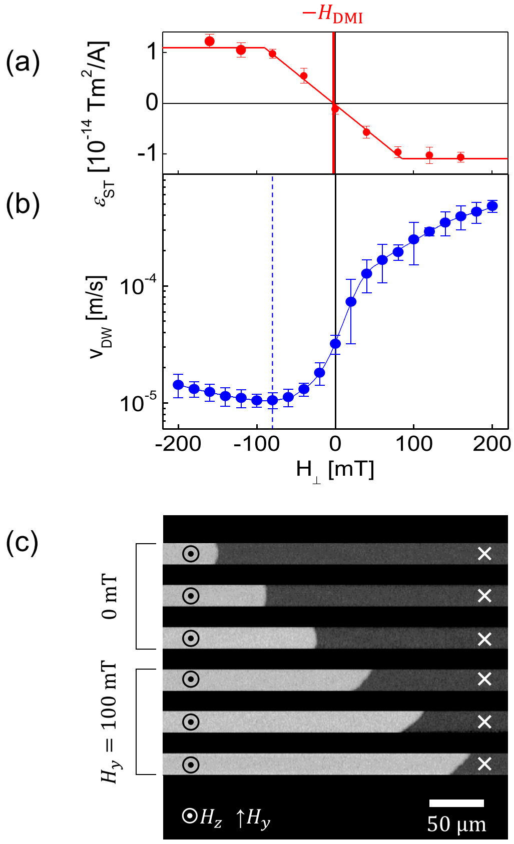

FIG. 5. (a) Plot of $\varepsilon_{\mathrm{ST}}$ as a function of H_x for sample III. The red vertical line indicates $-H_{\mathrm{DMI}}$. (b) Plot of v_{DW} as a function of $H_{\perp}$ for sample III. The blue dashed vertical line indicates H_x for the minimum v_{DW}. (c) Image of the domains and DW for the microwire-patterned sample III. The first three and last three images show the propagating domain without and with application of H_y, respectively.

case of $H_{\mathrm{DMI}} < 0$, whose sign is identical to that of sample I. It is clear from the figure that the counterclockwise DW tilting is well reproduced in accordance to the experimental observations.

It is also experimentally confirmed that, for the case of $H_{\mathrm{DMI}} = 0$, the DW tilting does not take place, as expected. Figure 4(a) is the plot of v_{DW} with respect to $H_{\perp}$ for sample II and reveals that this sample has negligible H_{DMI}. Due to the symmetric v_{DW} variation around $H_{\perp} = 0$, the upper and lower parts of the DW move with the same speed irrespective of the sign of $H_{\perp}$. Therefore, the DW keeps basically the same shape of the symmetric circular arcs even after application of H_y as seen in Fig. 4(b).

D. DW tilting induced by chirality-induced antisymmetry in v_{DW}

Until now, we have investigated the DW tilting for the case of symmetric v_{DW} variation induced by the DMI. However, very recently, many groups have uncovered the existence of the asymmetric v_{DW} variation [16–22]. Here, we explore the effects of such asymmetric v_{DW} variation on the DW tilting mechanism. For this purpose, the DW tilting is observed from a sample that has nearly zero H_{DMI}, but exhibits clear asymmetric v_{DW} variation. Figure 5(b) shows the plot of measured v_{DW} with respect to $H_{\perp}$ for sample III. The results clearly show that the present sample exhibits asymmetric v_{DW} variation, in contrast again to the symmetric variation of sample II. Such asymmetric v_{DW} variation is demonstrated to be caused by the chirality-induced antisymmetry in v_{DW} [22], of which origin may attribute to the chiral damping [17,18] or asymmetric DW width variation [19], even without the DMI.

Since v_{DW} does not symmetrically vary with respect to $H_{\perp}$ for sample III, H_{DMI} cannot be determined from the $v_{\mathrm{DW}}(H_{\perp})$ curve. Therefore, we introduce another independent DMI-determination technique, which measures the spin torque efficiency as a function of $H_{\perp}$. Figure 5(a) plots the spin-torque efficiency $\varepsilon_{\mathrm{ST}}$ with respect to $H_{\perp}$ for sample III [28,29]. Since the plot shows the antisymmetric behavior, it is worthwhile to note that $\varepsilon_{\mathrm{ST}}$ is mainly attributed by the spin-orbit torque efficiency $\varepsilon_{\mathrm{SOT}}$ (i.e., $\varepsilon_{\mathrm{ST}} \approx \varepsilon_{\mathrm{SOT}}$) for the sample III [30]. According to Refs. [29,30], $\varepsilon_{\mathrm{ST}}$ depends on the DW chirality, providing a relation that $\varepsilon_{\mathrm{ST}} \propto \cos\psi$, where ψ is the angle of the magnetization at the DW center. Therefore, the intercept to the abscissa (i.e., $\varepsilon_{\mathrm{ST}} = 0$, represented by red vertical arrow) in Fig. 5(a) indicates the Bloch-type DW ($\psi = \pi/2$), where H_{DMI} is exactly compensated with H_x, i.e., $H_x = -H_{\mathrm{DMI}}$. The plot thus indicates that H_{DMI} of the present sample is nearly zero ($=5 \pm 5$ mT), similar to sample II. It is worthwhile to note that $H_x \cong -80$ mT for the minimum v_{DW} (blue dashed vertical line) is largely shifted from $H_x = -H_{\mathrm{DMI}}$. This large shift reminds us that appropriate H_{DMI} cannot be determined unless one carefully considers the chirality-induced antisymmetry in v_{DW} [16–22].

Very interestingly, in contrast to the absence of the DW tilting in sample II, this sample exhibits clear DW tilting as shown by Fig. 5(c), despite both samples having nearly zero H_{DMI}. Therefore, one can deduce that the DW tilting can be also generated by the chirality-induced antisymmetry in v_{DW} [16–22], even without the DMI. Reminding that the DW tilting is induced by the DW speed difference between the upper and lower parts of the curved DW, one can explain the observed DW tilting with the same analogy. Since v_{DW} with $H_\perp > 0$ is faster than v_{DW} with $H_\perp < 0$, which is opposite to that of sample I [Fig. 1(b)], the direction of the DW tilting of the present sample should be also opposite to that of sample I. The present sample thus exhibits clockwise DW tilting, as confirmed by the experimental observation from Fig. 5(b). Therefore, it is general to conclude that the DW tilting is generated by the v_{DW} difference between the upper and lower parts of the DW [i.e., between $v_{\mathrm{DW}}(+H_\perp)$ and $v_{\mathrm{DW}}(-H_\perp)$], whatever the origin of the difference—either the DMI (sample I) [8] or chirality-induced antisymmetry in v_{DW} (sample III) [16–22]—is.

E. Direct correlation between DW tilting angle and v_{DW} asymmetry

Finally, as a general case, we examine the case that the sample has both a sizable DMI and chirality-induced v_{DW} variation. Figure 6(a) plots $\varepsilon_{\mathrm{ST}}$ with respect to H_x for sample IV. The typical spin-orbit torque-driven behavior again quantifies $H_{\mathrm{DMI}} = -107 \pm 7$ mT. This sample exhibits also the chirality-induced asymmetric v_{DW} variation with respect to $H_\perp$ as shown by Fig. 6(b).

For this sample, drastic change on the DW tilting is observed depending on the magnitude of H_y; even the tilting direction is reversed as shown by Fig. 6(c). For detailed investigation, the DW tilting angle θ_{tilt} was measured as a function of H_y and then was plotted by Fig. 6(d). The plot shows that θ_{tilt} is reversed across a threshold magnetic field H_y^{th} (green vertical line). Therefore, a counterclockwise DW tilting appears when $H_y < H_y^{\mathrm{th}}$, otherwise a clockwise DW tilting appears.

The present peculiar results can be explained by considering the asymmetric v_{DW} variation with respect to $H_\perp$. Recalling that $H_\perp$ at the upper part of the DW is opposite to the lower part of the circular DW arc as shown by Fig. 2(a), the initial difference Δv_{DW} of the DW speed between the upper and lower parts of the DW basically follows the relation $\Delta v_{\mathrm{DW}} = v_{\mathrm{DW}}(H_\perp) - v_{\mathrm{DW}}(-H_\perp)$. To visualize Δv_{DW}, $v_{\mathrm{DW}}(-H_\perp)$ is plotted by the gray dashed line in Fig. 6(b) together with $v_{\mathrm{DW}}(H_\perp)$ of the symbols with blue line. Then, Δv_{DW} corresponds to the vertical difference between these two lines (purple arrow). It is again seen from the figure that the sign of Δv_{DW} is reversed across a threshold magnetic field $H_\perp^{\mathrm{th}}$ (green vertical line). Thus, for the case that $H_\perp$ is smaller than $H_\perp^{\mathrm{th}}$, the DW rotates counterclockwise with $\Delta v_{\mathrm{DW}} < 0$ and vice versa, in accordance to the observation from Fig. 6(d). Figure 6(e) shows the plot of θ_{tilt} with respect to $\Delta(\ln v_{\mathrm{DW}})$ for sample IV. A clear correlation between θ_{tilt} and $\Delta(\ln v_{\mathrm{DW}})$ is the obvious evidence that the DW tilting is truly determined by the asymmetry of the v_{DW} variation.

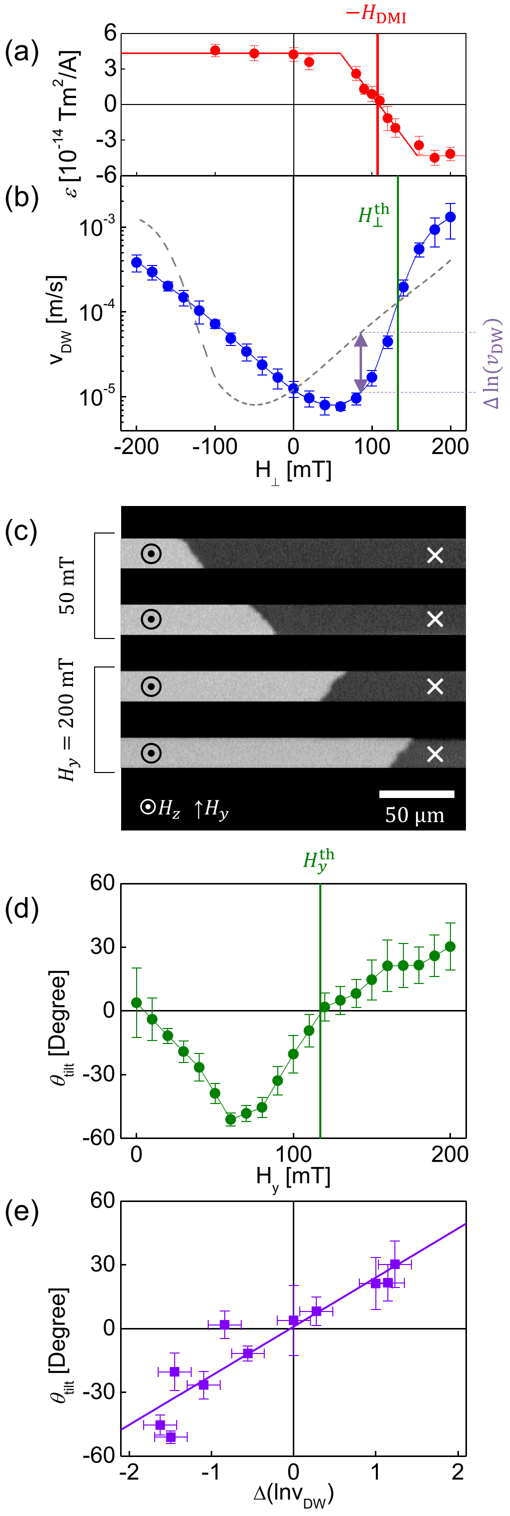

FIG. 6. (a) Plot of $\varepsilon_{\mathrm{ST}}$ as a function of H_x for sample IV. The red vertical line indicates $-H_{\mathrm{DMI}}$. (b) Plot of v_{DW} as a function of $H_\perp$ for sample IV. The gray dashed line shows $v_{\mathrm{DW}}(-H_\perp)$. The green vertical line indicates $H_\perp^{\mathrm{th}}$, where the blue and dashed-gray curves intersect. (c) Image of the domains and DW for the microwire-patterned sample IV. The first two and last two images show the propagating domain under the application of $H_y = 50$ mT and $H_y = 200$ mT, respectively. (d) Plot of θ_{tilt} as a function of H_y. The green vertical line indicates H_y^{th}, where $\theta_{\mathrm{tilt}} = 0$. (e) Plot of θ_{tilt} with respect to $\Delta(\ln v_{\mathrm{DW}})$. The best linear fitting ($R^2 = 0.87$) is presented by the purple solid line.

IV. DISCUSSION

There remain several challenging issues towards full analytic description of the DW tilting angle θ_{tilt}. First, we consider the effect of $H_{\parallel}$. Since the sign and magnitude of $H_{\parallel}$ at both the upper and lower parts of the DW are the same as seen by Fig. 2(a), the difference should be mainly attributed to the opposite sign of $H_{\perp}$. For the case near the Bloch-type configuration, by applying the first-order Taylor expansion with respect to ψ, the DW energy density σ_{DW} becomes $\sigma_0 - \frac{1}{2}\pi\lambda M_{\text{S}}[(H_{\perp} + H_{\text{DMI}})^2 + 2H_{\text{S}}|H_{\parallel}|]/(H_{\text{S}} + |H_{\parallel}|)$ with the first leading terms of $H_{\perp}$ and $H_{\parallel}$, where the DW anisotropy field H_{S} is defined as $4K_{\text{D}}/\pi M_{\text{S}}$. The difference $\Delta\sigma_{\text{DW}}$ is then given by $-\pi\lambda M_{\text{S}} H_{\perp}^{+}[H_{\text{DMI}}/(H_{\text{S}} + |H_{\parallel}|)]$, where $H_{\perp}^{+}$ denotes $H_{\perp}$ at the upper parts of the DW. Note that $\Delta\sigma_{\text{DW}}$ is directly proportional to $H_{\perp}^{+}$, but less sensitive to $H_{\parallel}$. Similarly, for the case near the Néel-type configuration with a large H_{DMI}, $\Delta\sigma_{\text{DW}} \cong -\frac{1}{2}\pi\lambda M_{\text{S}} H_{\parallel}[H_{\parallel}/(H_{\text{DMI}} + H_{\perp})]$, which is negligible due to the small ratio of $H_{\parallel}/(H_{\text{DMI}} + H_{\perp})$. Therefore, one can conclude that $H_{\parallel}$ has negligible effect and the DW tilting is mainly governed by $H_{\perp}$.

Second, though the mechanism discussed with Δv_{DW} successfully explains the direction of the DW tilting as seen in Fig. 6(e), it is worthwhile to consider that there should be a restoring force to reach an equilibrium state with a finite θ_{tilt}. It is clear that the DW tension induces the restoring force [31], since the DW tension energy increases as the DW tilts. The role of the tension-induced force can be roughly estimated as follows. The DW tension energy E_{tension} is given by $E_{\text{tension}} = \sigma_{\text{DW}} wt \sec\theta_{\text{tilt}}$ as a function of θ_{tilt} within the assumption of a straight DW, where w and t are the wire width and thickness, respectively. When the DW tilts from θ_{tilt} to $\theta_{\text{tilt}} + \delta\theta$, the upper and lower parts of the DW has the variation $\delta E_{\text{tension}}^{\pm}$ as given by $\frac{1}{2}\sigma_{\text{DW}} wt\delta\theta \sec\theta_{\text{tilt}} \tan\theta_{\text{tilt}}$, where the superscripts, $+$ and $-$, indicate the upper and lower parts of the DW, respectively. Similarly, the Zeeman energy has the variation $\delta E_{\text{Zeeman}}^{\pm}$ by $\pm\frac{1}{2}M_{\text{S}} H_z w^2 t\delta\theta \sec^2\theta_{\text{tilt}}$. Comparing these two energy variations, one can get the relation of the tension-induced effective magnetic field $H_z^{\pm}$ as $H_z^{\pm} = \pm\sigma_{\text{DW}} \sin\theta_{\text{tilt}}/M_{\text{S}} w$. For the case of a counterclockwise DW tilting (i.e., $\theta_{\text{tilt}} > 0$), a positive H_z^{+} enhances the DW speed of the upper part while a negative H_z^{-} reduces the DW speed of the lower part, resulting in clockwise rotation and vice versa. Therefore, the DW tension exerts a restoring force on the DW. The equilibrium θ_{tilt} is then determined by the steady-state condition, i.e.,$v_{\text{DW}}(H_{\perp}^{+}, H_z + H_z^{+}) = v_{\text{DW}}(H_{\perp}^{-}, H_z + H_z^{-})$. Though an analytic solution of the present condition is not available due to the yet unknown nature of the chirality-induced v_{DW} asymmetry, one can get the empirical solution by analyzing the two-dimensional map of $v_{\text{DW}}(H_{\perp}, H_z)$ measured as a function of $H_{\perp}$ and H_z.

V. CONCLUSION

In summary, the experimental results clearly manifest that the DW tilting is triggered by the DW pinning at the structure edge, which is in contradiction to a naive prediction based on the energy minimization. The direction of the DW tilting is governed by the DW speed asymmetry, irrespective of the origins of the asymmetry, either the DMI [8] or chirality-induced mechanisms [16–22]. The angle of the equilibrium DW tilting is then determined by the counterbalance between the DW speed asymmetry and the DW tension. The present observation indicates that the DW dynamics, rather than the DW energy minimization, plays a decisive role in practical magnetic structures with finite edge roughness.

ACKNOWLEDGMENTS

This work was supported by grants from National Research Foundations of Korea (NRF) funded by the Ministry of Science, ICT and Future Planning of Korea (MSIP) (Grants No. 2015R1A2A1A05001698 and No. 2015M3D1A1070465). Y.-K.P. and B.-C.M. were supported by the National Research Council of Science & Technology (NST) (Grant No. CAP-16-01-KIST) by the Korea government (MSIP). D.-H.K. was supported from Overseas researcher under a Postdoctoral Fellowship of Japan Society for the Promotion of Science (JSPS) (Grant No. P16314).

---

[1] I. Dzyaloshinsky, J. Phys. Chem. Solids **4**, 241 (1958).
[2] T. Moriya, Phys. Rev. **120**, 91 (1960).
[3] A. Fert, V. Cros, and J. Sampaio, Nat. Nanotechnol. **8**, 152 (2013).
[4] T. Schulz, R. Ritz, A. Bauer, M. Halder, M. Wagner, C. Franz, C. Pfleiderer, K. Everschor, M. Garst, and A. Rosch, Nat. Phys. **8**, 301 (2012).
[5] S. Mühlbauer, B. Binz, F. Jonietz, C. Pfleiderer, A. Rosch, A. Neubauer, R. Georgii, and P. Böni, Science **323**, 915 (2009).
[6] A. Thiaville, S. Rohart, E. Jué, V. Cros, and A. Fert, Europhys. Lett. **100**, 57002 (2012).
[7] M. Heide, G. Bihlmayer, and S. Blügel, Phys. Rev. B **78**, 140403(R) (2008).
[8] S.-G. Je, D.-H. Kim, S.-C. Yoo, B.-C. Min, K.-J. Lee, and S.-B. Choe, Phys. Rev. B **88**, 214401 (2013).
[9] A. Hrabec, N. A. Porter, A. Wells, M. J. Benitez, G. Burnell, S. McVitie, D. McGrouther, T. A. Moore, and C. H. Marrows, Phys. Rev. B **90**, 020402(R) (2014).
[10] D.-Y. Kim, D.-H. Kim, J. Moon, and S.-B. Choe, Appl. Phys. Lett. **106**, 262403 (2015).
[11] D.-S. Han, N.-H. Kim, J.-S. Kim, Y. Yin, J.-W. Koo, J. Cho, S. Lee, M. Klaui, H. J. M. Swagten, B. Koopmans, and C.-Y. You, Nano Lett. **16**, 4438 (2016).
[12] J. Cho, N.-H. Kim, S. Lee, J.-S. Kim, R. Lavrijsen, A. Solignac, Y. Yin, D.-S. Han, N. J. J. van Hoof, H. J. M. Swagten, B. Koopmans, and C.-Y. You, Nat. Commun. **6**, 7635 (2015).
[13] O. Boulle, S. Rohart, L. D. Buda-Prejbeanu, E. Jué, I. M. Miron, S. Pizzini, J. Vogel, G. Gaudin, and A. Thiaville, Phys. Rev. Lett. **111**, 217203 (2013).
[14] E. Jué, A. Thiaville, S. Pizzini, J. Miltat, J. Sampaio, L. D. Buda-Prejbeanu, S. Rohart, J. Vogel, M. Bonfim, O. Boulle, S.

Auffret, I. M. Miron, and G. Gaudin, Phys. Rev. B **93**, 014403 (2016).

[15] F. C. Ummelen, N. H. J. Wilting, R. Lavrijsen, H. J. M. Swagten, and B. Koopmans, *Dzyaloshinskii-Moriya Interaction Probed by Domain-wall Tilting*, The 9th International Symposium on Metallic Multilayers, Uppsala University, Uppsala, Sweden (2016).

[16] R. Lavrijsen, D. M. F. Hartmann, A. van den Brink, Y. Yin, B. Barcones, R. A. Duine, M. A. Verheijen, H. J. M. Swagten, and B. Koopmans, Phys. Rev. B **91**, 104414 (2015).

[17] E. Jué, C. K. Safeer, M. Drouard, A. Lopez, P. Balint, L. Buda-Prejbeanu, O. Boulle, S. Auffret, A. Schuhl, A. Manchon, I. M. Miron, and G. Gaudin, Nat. Mater. **15**, 272 (2016).

[18] C. A. Akosa, I. M. Miron, G. Gaudin, and A. Manchon, Phys. Rev. B **93**, 214429 (2016).

[19] D.-Y. Kim, D.-H. Kim, and S.-B. Choe, Appl. Phys. Express **9**, 053001 (2016).

[20] D.-H. Kim, S.-C. Yoo, D.-Y. Kim, B.-C. Min, and S.-B. Choe, arXiv:1608.01762.

[21] D. Lau, V. Sundar, J.-G. Zhu, and V. Sokalski, Phys. Rev. B **94**, 060401(R) (2016).

[22] D.-Y. Kim, M.-H. Park, Y.-K. Park, J.-S. Kim, Y.-S. Nam, H.-C. Choi, D.-H. Kim, S.-G. Je, B.-C. Min, and S.-B. Choe, NPG Asia Mater. **10**, e464 (2018).

[23] F. Cayssol, D. Ravelosona, C. Chappert, J. Ferré, and J. P. Jamet, Phys. Rev. Lett. **92**, 107202 (2004).

[24] A. Thiaville, Y. Nakatani, J. Miltat, and Y. Suzuki, Europhys. Lett. **69**, 990 (2005).

[25] S. Lemerle, J. Ferré, C. Chappert, V. Mathet, T. Giamarchi, and P. Le Doussal, Phys. Rev. Lett. **80**, 849 (1998).

[26] G. Blatter, M. V. Feigel'man, V. B. Geshkenbein, A. I. Larkin, and V. M. Vinokur, Rev. Mod. Phys. **66**, 1125 (1994).

[27] A. I. Larkin and Y. N. Ovchinnikov, J. Low Temp. Phys. **34**, 409 (1979).

[28] J.-C. Lee, K.-J. Kim, J. Ryu, K.-W. Moon, S.-J. Yun, G.-H. Gim, K.-S. Lee, K.-H. Shin, H.-W. Lee, and S.-B. Choe, Phys. Rev. Lett. **107**, 067201 (2011).

[29] P. P. J. Haazen, E. Murè, J. H. Franken, R. Lavrijsen, H. J. M. Swagten, and B. Koopmans, Nat. Mater. **12**, 299 (2013).

[30] S.-G. Je, S.-C. Yoo, J.-S. Kim, Y.-K. Park, M.-H. Park, J. Moon, B.-C. Min, and S.-B. Choe, Phys. Rev. Lett. **118**, 167205 (2017).

[31] K.-W. Moon, J.-C. Lee, S.-G. Je, K.-S. Lee, K.-H. Shin, and S.-B. Choe, Appl. Phys. Express **4**, 043004 (2011).